

Polarization impacts on the water-leaving radiance retrieval from above-water radiometric measurements

Tristan Harmel,^{1,*} Alexander Gilerson,² Alberto Tonizzo,² Jacek Chowdhary,³
Alan Weidemann,⁴ Robert Arnone,⁵ and Sam Ahmed²

¹Laboratoire d'Océanographie de Villefranche, Centre national de la recherche scientifique (CNRS),
Université Pierre et Marie Curie, Villefranche-sur-Mer, France

²Optical Remote Sensing Laboratory, City College of the City University of New York, New York 10031, USA

³Department of Applied Physics and Applied Mathematics, Columbia University, New York 10025, USA

⁴Naval Research Laboratory, Stennis Space Center, Mississippi 39529, USA

⁵University of Southern Mississippi, Mississippi 39529, USA

*Corresponding author: harmel@obs-vlfr.fr

Received 25 September 2012; revised 5 November 2012; accepted 5 November 2012;
posted 8 November 2012 (Doc. ID 176895); published 5 December 2012

Above-water measurements of water-leaving radiance are widely used for water-quality monitoring and ocean-color satellite data validation. Reflected skylight in above-water radiometry needs to be accurately estimated prior to derivation of water-leaving radiance. Up-to-date methods to estimate reflection of diffuse skylight on rough sea surfaces are based on radiative transfer simulations and sky radiance measurements. But these methods neglect the polarization state of the incident skylight, which is generally highly polarized. In this paper, the effects of polarization on the sea surface reflectance and the subsequent water-leaving radiance estimation are investigated. We show that knowledge of the polarization field of the diffuse skylight significantly improves above-water radiometry estimates, in particular in the blue part of the spectrum where the reflected skylight is dominant. A newly developed algorithm based on radiative transfer simulations including polarization is described. Its application to the standard Aerosol Robotic Network-Ocean Color and hyperspectral radiometric measurements of the 1.5-year dataset acquired at the Long Island Sound site demonstrates the noticeable importance of considering polarization for water-leaving radiance estimation. In particular it is shown, based on time series of collocated data acquired in coastal waters, that the azimuth range of measurements leading to good-quality data is significantly increased, and that these estimates are improved by more than 12% at 413 nm. Full consideration of polarization effects is expected to significantly improve the quality of the field data utilized for satellite data validation or potential vicarious calibration purposes. © 2012 Optical Society of America

OCIS codes: 010.0010, 280.0280, 010.4450, 010.1320.

1. Introduction

Spectral water-leaving radiance, as measured by in-water or above-water instrumentation or from satellites, is operationally utilized for ocean and

coastal water-quality monitoring as well as in various applications such as ecological or climatic models, oceanic impacts of the global change, fisheries, and so forth [1]. However, the estimation of the water-leaving radiance from satellites remains complex due to the presence of the atmosphere between the water body and the sensor [2]. As a result, this estimation needs sophisticated data processing,

1559-128X/12/358324-17\$15.00/0

© 2012 Optical Society of America

201 21228005

which is particularly challenging in coastal water areas. A mandatory effort is then dedicated to validation of the satellite retrievals on the basis of comparison with field-truth measurements [3–5].

The water-leaving radiance can be derived from underwater or above-water instrumentation. In underwater methods, the upwelling radiance and downwelling irradiance are measured at several depths. These data are then extrapolated to the surface level and propagated upward through the sea–air interface. Accuracy in the retrieved water-leaving radiance depends on exposure errors, such as ship shadows, instrument self-shading, biological fouling, and so forth. Moreover, in turbid waters, or in the red part of the spectrum, where the absorption coefficient is large, the extrapolation to the surface may be particularly difficult [6].

In contrast, the above-water method seeks to derive the water-leaving radiance from radiometric measurement of the sea surface from the deck of a boat or from instrumentation installed on a platform. At the same time, the downwelling irradiance is directly measured or estimated from sky measurements in order to normalize the sea measurements [7,8]. The sun and sky light, which have undergone specular reflection on the sea surface in the direction toward the radiometer, must be subtracted prior to water-leaving radiance estimation. This procedure corresponds to the most critical step in above-water radiometry achievement, as recently discussed [9–11]. To handle this issue, it was first proposed to remove the reflected sky light by subtracting the sky radiance measured in the direction for which the sky light would be reflected toward the sensor by a flat surface after multiplication by the scalar Fresnel coefficient (i.e., first term of the Fresnel matrix) at the same angle [12]. This approach was then extended to account for integration of the scalar Fresnel coefficient over the radiometer field of view [13]. At the same period, typical values of the reflection factor of the rough sea surface were derived from radiative transfer computations [14] and have been used to date in most of the above-water radiometry programs [4,9,15]. However, it was assumed in all those methods that polarization features occurring during light reflection on the sea surface can be neglected and the polarization state of the incident sky light is not accounted for. Other studies made use of the polarization properties of the specular reflection on the sea surface to minimize the impact of the reflected sky light on the measurements by using a polarizer and appropriate viewing configurations [16–18]. However, no strict consideration of the polarization state of the incident sky light was taken into account.

Solar radiation is initially unpolarized when entering the Earth's atmosphere. Yet natural sunlight is scattered by aerosols and molecules, refracted and reflected at the atmosphere–ocean interface, and further scattered by hydrosols and water molecules. As a result of these interactions, solar radiation becomes partially polarized, and the resulting

polarization field depends on the optical properties of the atmosphere–ocean system. Thus, the downwelling skylight might be highly polarized [19], and its polarization state is dependent on the actual optical properties of the atmosphere [20–22]. Accordingly, the reflected sky light on the sea surface can be expected to be itself impacted by the polarization field of the atmosphere. The main goal of this study is then to investigate the effects of polarization on the sea surface signal and, in turn, on the performances of the water-leaving radiance estimation from above-water measurements.

This paper is organized as follows. The following section describes the radiative transfer modeling of the sky light reflection on a rough sea surface and theoretically discusses the impact of polarization on the estimation of the surface reflectance and water-leaving radiance. The third section summarizes the characteristics of the Long Island Sound Coastal Observatory (LISCO), which combines collocated multi- and hyperspectral radiometers installed on a platform. Measurements of the sky and sea radiances and of the downwelling irradiance have been acquired since October 2009 for water-leaving radiance estimation and aerosol determination via the Aerosol Robotic Network (AERONET) program [23]. The fourth section describes the polarization-based correction scheme for water-leaving radiance retrieval from above-water measurements. Results of applications to the LISCO data are presented and discussed based on comparison of collocated field data. Conclusive remarks and perspectives are given in the last section.

2. Theoretical Background

A. Above-Water Signal

The total bidirectional reflectance just above the sea surface is defined at a given wavelength as follows:

$$\rho_t(\theta_s, \theta_v, \phi) = \frac{\pi L_t(\theta_s, \theta_v, \phi)}{E_s(\theta_s)}, \quad (1)$$

where L_t is the upward radiance measured from an above-water radiometer pointing at the sea with a given viewing configuration defined by the solar zenith angle θ_s , the viewing zenith angle θ_v , and the relative azimuth between the Sun and the radiometer ϕ . E_s is the downwelling total irradiance at the sea level just above the surface. In like manner, the definition of Eq. (1) can be extended to the Stokes vector, expressed in reflectance unit, $S = [\rho, q, u, v]^T$, which describes electromagnetic radiation, including its polarization state, in terms of directly measurable quantities; the superscript T stands for the transpose of the vector.

The Stokes vector is defined in this paper with respect to the reference frame determined by the viewing direction of the above-water radiometer and the local zenith (i.e., the local meridian plane). For incoherent light, Stokes vectors are additive, which enables us to decompose the above-water signal at

a given wavelength and a given viewing configuration as follows:

$$S_t = S_g + S_{\text{surf}} + S_{wc} + S_w. \quad (2)$$

S_t , S_g , S_{surf} , S_{wc} , and S_w stand for the Stokes vectors of the total, sun glint, sea surface reflection of sky light, foam, and water-leaving components of the above-water signal, respectively. More precisely, S_g is the contribution arising from specular reflection of direct sunlight on the sea surface, S_{surf} is the contribution generated by specular reflection of atmospherically scattered light on the sea surface, S_{wc} is the contribution arising from sunlight and sky light reflected by whitecap-covered areas of the sea surface, and S_w is the contribution of underwater light scattered toward the above-water radiometer after propagation through the sea surface.

Generally, the data processing of above-water measurement permits filtering out any data contaminated by prohibitive amounts of sun glint or foam contribution [4,24]. Consequently, this study will be mostly dedicated to analyzing the surface reflection of diffuse skylight and the water-leaving contribution, and Eq. (2) can be reformulated as

$$S_t = S_{\text{surf}} + S_w + \varepsilon, \quad (3)$$

where the term ε accounts for residual sun glint or foam that might remain even after data filtering. In neglecting ε , the main issue to solve in above-water radiometry is to accurately estimate S_{surf} in order to retrieve S_w from measurements.

B. Fresnel's Reflection Matrix

The Stokes vector of the surface contribution just above water can be first calculated for a flat surface. This computation is based on Fresnel's reflection matrix, for which a beam of light is reflected toward the sensor. Let n be the complex refractive index of sea water relative to the air index and θ_i be the incident angle of a beam of light illuminating the surface, which is equal to half the phase angle (i.e., complementary of the scattering angle). The angle θ_i can be defined with respect to the above-water viewing configuration for any orientation of the flat surface considered:

$$\cos 2\theta_i = -\cos \theta' \cos \theta_v - \sin \theta' \sin \theta_v \cos \phi', \quad (4)$$

with θ' and ϕ' the zenith angle and the relative azimuth with the viewing direction of the incident beam considered, and θ_v the viewing zenith angle. For more details on the geometrical parameters used, the reader is referred to Fig. 1. Note that the relative azimuth ϕ' is equal to 0° when the source of the light beam being considered and the sensor are in opposition, following the convention commonly used in above-water radiometry.

For a given incident angle, the Fresnel's reflection matrix is expressed in the plane defined by the Sun

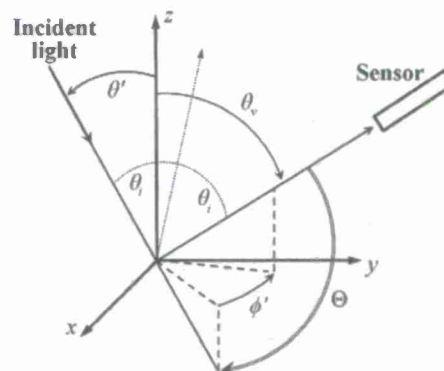


Fig. 1. Definition of the viewing geometry convention used: θ_i is the incident angle of a beam of light illuminating the surface, θ' and ϕ' are the zenith angle and the relative azimuth with the viewing direction of the incident beam considered, θ_v is the viewing zenith angle, and Θ is the scattering angle.

and satellite directions, that is, the plane of incidence, as follows:

$$r_f(\theta_i) = \frac{1}{2} \begin{pmatrix} r_{\parallel} r_{\parallel}^* + r_{\perp} r_{\perp}^* & r_{\parallel} r_{\parallel}^* - r_{\perp} r_{\perp}^* & 0 & 0 \\ r_{\parallel} r_{\parallel}^* - r_{\perp} r_{\perp}^* & r_{\parallel} r_{\parallel}^* + r_{\perp} r_{\perp}^* & 0 & 0 \\ 0 & 0 & \Re\{2r_{\parallel} r_{\perp}^*\} & \Im\{2r_{\parallel} r_{\perp}^*\} \\ 0 & 0 & -\Im\{2r_{\parallel} r_{\perp}^*\} & \Re\{2r_{\parallel} r_{\perp}^*\} \end{pmatrix}, \quad (5)$$

where the superscript $*$ stands for the complex conjugate. The terms r_{\perp} and r_{\parallel} are the components perpendicular and parallel to the plane of incidence, respectively, defined by

$$r_{\perp} = \frac{\cos \theta_i - \sqrt{n^2 - \sin^2 \theta_i}}{\cos \theta_i + \sqrt{n^2 - \sin^2 \theta_i}},$$

$$r_{\parallel} = \frac{n^2 \cos \theta_i - \sqrt{n^2 - \sin^2 \theta_i}}{n^2 \cos \theta_i + \sqrt{n^2 - \sin^2 \theta_i}}. \quad (6)$$

The r_f matrix has been defined with respect to the incident plane. In order to formulate the Stokes vector originating from specular reflection with respect to the reference plane, the r_f matrix must be reprojected accordingly to get the proper reflection matrix R_f :

$$R_f(\theta_i) = L(\pi - \sigma_2) r_f(\theta_i) L(-\sigma_1), \quad (7)$$

where L is the rotation matrix for the angles σ_1 and σ_2 defined with respect to the solar and viewing zenith angles and the scattering angle Θ (given by $\pi - 2\theta_i$):

$$\begin{aligned}\cos \sigma_1 &= \frac{\cos \theta_v - \cos \theta' \cos \Theta}{\sin \theta' \sin \Theta}, \\ \cos \sigma_2 &= \frac{\cos \theta' - \cos \theta_v \cos \Theta}{\sin \theta_v \sin \Theta}.\end{aligned}\quad (8)$$

In the case of a flat surface, the Stokes vector S_{surf} can be therefore expressed as

$$S_{\text{surf}}(\theta_s, \theta_v, \phi) = R_f(\theta_i) S_{\text{sky}}(\theta_s, \theta' = \pi - \theta_v, \phi), \quad (9)$$

where S_{sky} is the Stokes vector of the diffuse sky light as measured by a sensor looking upward with an angle θ_v . As a result, the component ρ_{surf} , corresponding to the reflectance of the sea surface, is obtained by

$$\rho_{\text{surf}} = R_{11}\rho_{\text{sky}} + R_{12}q_{\text{sky}} + R_{13}u_{\text{sky}} + R_{14}v_{\text{sky}}, \quad (10)$$

where the terms R_{11} to R_{14} are the components of the first row of the Fresnel matrix. It is worth noting that the fourth component v_{sky} of S_{sky} is very low and can generally be neglected in comparison to the first three components [25–27]. The respective values of R_{11} , R_{12} , and R_{13} are therefore of paramount importance in the generation of the upwelling signal of the sea surface contribution as measured by above-water instrumentation.

The Fresnel matrix component R_{11} and the components R_{12} and R_{13} normalized by R_{11} are displayed in Fig. 2 for a given viewing angle equal to 40° and solar angle ranging from 0° to 70° for the full azimuth range. It can be readily seen in this figure that the term R_{11} is virtually constant and equal to 0.021 for a large range of azimuth roughly comprised between -60° and 60° . Regarding the rest of the azimuth range, this term is strongly dependent on the solar angle and can reach values up to 0.04. More interestingly, the contribution of R_{12} and R_{13} are far from being negligible in comparison to R_{11} . In particular, the values of these two terms can correspond to up to 50% of the R_{11} values, as shown by the ratios R_{12}/R_{11} and R_{13}/R_{11} , for almost the whole range of azimuths. In conclusion, the nondiagonal terms of the Fresnel

matrix must be taken into account to accurately compute the bidirectional reflectance of the sea surface, even for a flat surface.

In general, the sea surface is roughened by the wind. As a result, a myriad of reflecting facets might reflect skylight originating from any direction of the sky. Various contributions of the skylight will reach the above-water sensor due to specular reflection from waves and wavelets at the sea surface. Following Cox and Munk [28–30], the ocean surface can be modeled based on a distribution of small facets that are oriented following a near-Gaussian distribution. In this model, the statistical distribution of the orientation of the facets leading to sunlight reflection toward the radiometer is given with respect to the viewing configuration as well as the wind speed and azimuth, denoted as ws and ϕ_{wind} , respectively. Thus, the Stokes vector of the sea surface contribution S_{surf} can be written as (see [31], for instance)

$$\begin{aligned}S_{\text{surf}} &= \int_{\theta'=0}^{\pi/2} \int_{\phi'=0}^{2\pi} C_s \frac{R_f(\theta_i)}{4 \cos \theta_v \cos^4 \theta_n} p(\theta', \theta_v, \phi'; ws, \phi_{\text{wind}}) \\ &\times S_{\text{sky}}(\theta_s, \theta', \phi') d\theta' d\phi'.\end{aligned}\quad (11)$$

The term θ_n is the angle between the zenith and the normal to the facets, and θ_i is computed from Eq. (4). The term p is the wave slopes distribution, and C_s accounts for the shadowing effects of the waves [32] and depends on the viewing geometry and the wind speed (see [31] for the complete expression of this term). To solve Eq. (11) a complete knowledge of the term S_{sky} , for any incident direction, is needed. Recent instrumental developments have enabled us to measure this term for the radiance parameter (i.e., first component of the Stokes vector) and the polarization components [19,33], but further efforts are still to be done for their operational use in above-water radiometry. A practical solution to fully derive S_{surf} is therefore to solve the radiative transfer equation, which can be easily achieved based on the numerous codes available, including polarization computation; see [27,31,34–37], to cite only a few.

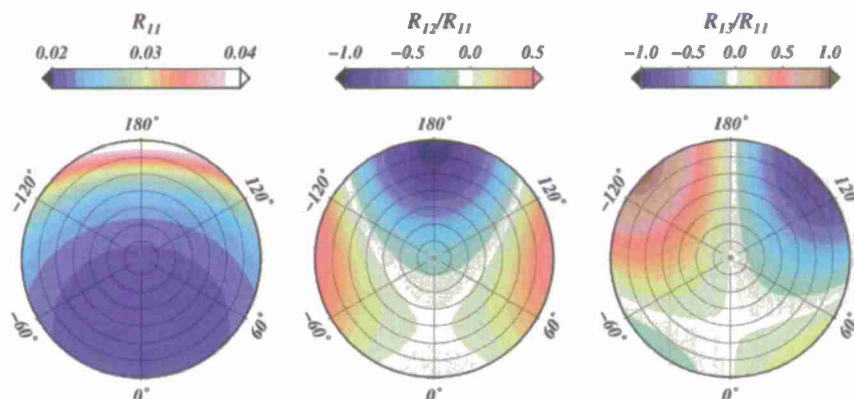


Fig. 2. (Color online) Fresnel coefficient R_{11} and the Fresnel coefficients R_{12} and R_{13} normalized by R_{11} . The viewing zenith angle is set to 40° . The concentric circles represent the solar zenith angles by step of 10° (from 0° to 70°), and angles in the polar diagrams represent the relative azimuth with the Sun. By convention, the azimuth is equal to 0° when the Sun and the sensor are in opposition.

C. Estimation of the Water-leaving Reflectance

In above-water radiometry, the standard way to derive the sea surface reflectance is based on sky radiance measurements L_{sky} acquired at the same time as the total sea radiance L_t [4,7,38]. In order to remove, or at least minimize, the impact of the sun glint on the measured sea radiance, the average L_t^* is computed over a fixed percentage, typically 5%, of the lowest values of sea radiance measured during the acquisition sequence [7,38]. The water-leaving radiance L_w is then computed as

$$L_w(\theta_s, \theta_v, \phi) = L_t^*(\theta_s, \theta_v, \phi) - f(\theta_s, \theta_v, \phi, ws) \times L_{\text{sky}}(\theta_s, \theta' = \pi - \theta_v, \phi). \quad (12)$$

The second term of the right-hand side of the equation is the estimate of the radiance resulting from diffuse skylight reflected off the sea surface. The coefficient $f(\theta_s, \theta_v, \phi, ws)$ is the sea surface-reflectance factor, which is dependent on sky condition, wind speed ws , and the viewing configuration. This term was parameterized from radiative transfer computation in neglecting the incident polarization field [14]. The water-leaving reflectance, ρ_w , is then obtained by multiplying L_w by π/E_s . In this study, we propose to replace the estimate of the sea surface signal by that computed through Eq. (11), which includes the impact of the polarization of sky light on the estimation of the water-leaving signal. Equation (12) can be then rewritten as

$$\rho_w(\theta_s, \theta_v, \phi) = \frac{\pi L_t^*(\theta_s, \theta_v, \phi)}{E_s} - \rho_{\text{surf}}(\theta_s, \theta_v, \phi). \quad (13)$$

The sea surface reflectance ρ_{surf} was simulated using Chowdhary's radiative transfer code [34] for a viewing angle of 40° , a solar zenith angle ranging from 0° to 90° by a step of about 1° for any azimuth value. In these computations, the wave slope distribution based on Cox and Munk parameterization was assumed including modeling of wave self-shadowing [32]. In addition, these simulations were achieved following two modalities: (1) in fully considering the impact of the polarization field occurring at the sea surface, referred to as $\rho_{\text{surf}}(\text{vector})$, and (2) in neglecting the polarization components of the Fresnel matrix (i.e., $R_{12} = R_{13} = 0$), referred to as $\rho_{\text{surf}}(\text{scalar})$. Note that under this assumption, the term $\rho_{\text{surf}}(\text{scalar})$ is equivalent to the term fL_{sky} of Eq. (12) used in the current correction methods. In comparing $\rho_{\text{surf}}(\text{vector})$ with $\rho_{\text{surf}}(\text{scalar})$, the importance of considering polarization in the estimation of the water-leaving reflectance can thus be inferred.

The simulations of $\rho_{\text{surf}}(\text{scalar})$ and $\rho_{\text{surf}}(\text{vector})$ at 550 nm are shown in Figs. 3(a) and 3(b) for two different azimuths, namely 90° and 135° , and three different aerosol optical thicknesses: 0, 0.1, and 0.2. Note that the microphysical properties of the aerosols also influence the signal reflected by the sea surface. For the sake of simplicity the results are

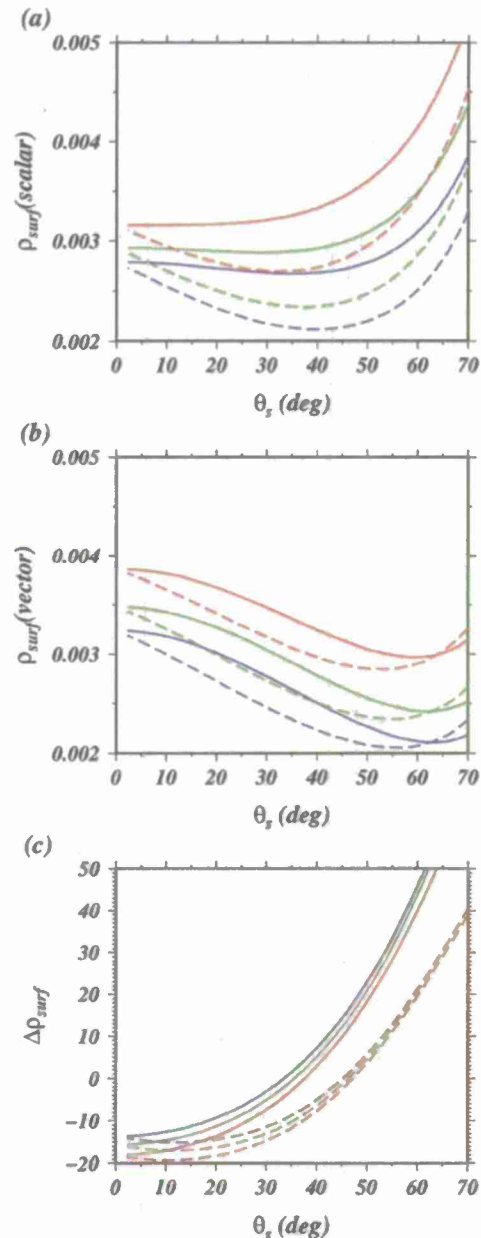


Fig. 3. (Color online) Sea surface reflectance at 550 nm for no-wind conditions with respect to the solar angle computed (a) in ignoring the polarization terms of the Fresnel matrix (i.e., $R_{12} = R_{13} = 0$) and (b) in fully considering polarization behavior of skylight reflection at the sea surface. (c) Relative difference expressed in percent between the sea surface reflectances displayed in (a) and (b). The results are shown for two different azimuths, namely 90° (solid curves) and 135° (dashed curves), and for different aerosol optical thicknesses: 0 (blue), 0.1 (green), and 0.2 (red).

uniquely shown for a fine-mode aerosol model characterized by a mean radius of $0.17 \mu\text{m}$ and a refractive index of 1.45. However, similar conclusions could be drawn irrespective of the aerosol model considered. When no polarization is considered in the computations [Fig. 3(a)], $\rho_{\text{surf}}(\text{scalar})$ is virtually constant with respect to the solar angle up to an angle of around 50° when an azimuth of 90° is considered. Beyond this solar angle, the estimated contribution

of the sea surface increases. In contrast, when polarization is considered [Fig. 3(b)], $\rho_{\text{surf}}(\text{vector})$ starts decreasing from solar angles around 15° and keeps on decreasing at important solar angles. The behavior of the sea surface reflectance with respect to the solar angle is therefore strongly impacted by the polarization state of the sky light beam hitting the sea surface.

A more quantitative view of the surface polarization effects can be obtained by computing the relative difference between $\rho_{\text{surf}}(\text{scalar})$ and $\rho_{\text{surf}}(\text{vector})$ as follows:

$$\Delta\rho_{\text{surf}} = 100 \frac{\rho_{\text{surf}}(\text{scalar}) - \rho_{\text{surf}}(\text{vector})}{\rho_{\text{surf}}(\text{vector})} \% \quad (14)$$

This relative difference is shown in Fig. 3(c). For an azimuth of 90° , which generally is used in above-water radiometry [4], the exhibited discrepancies between $\rho_{\text{surf}}(\text{scalar})$ and $\rho_{\text{surf}}(\text{vector})$ range between -20% at smaller solar angles up to over $+50\%$ beyond solar angles of 60° . This is consistent with expectations as the polarization terms R_{12} and R_{13} of the Fresnel matrix can attain 50% of the R_{11} value, as discussed before [see Fig. (2)]. Moreover, it is worth noticing that the downwelling sky radiance is in general highly polarized, with a degree of polarization that can exceed 60% for a large range of geometries in a purely molecular atmosphere [39,40]. As a result, even though aerosols' presence tends to diminish the degree of polarization, the high degree of polarization of the downwelling sky light enhances the importance of considering the full Fresnel matrix for estimation of the sea surface reflectance.

In contrast, the observed discrepancies between $\rho_{\text{surf}}(\text{scalar})$ and $\rho_{\text{surf}}(\text{vector})$ are significantly smaller when measurements are acquired at an azimuth of 135° . For this viewing configuration, the relative difference $\Delta\rho_{\text{surf}}$ remains negative and comprises between -25% and 0% over the full range of solar angles. On the other hand, it can be readily seen

in Fig. 3(c) that the effect of the aerosol loading is largely smoother than that of the azimuth used for observation. However, the aerosol optical thickness induces significant variation in the absolute surface reflected signal [see Fig. 3(b)] and must also be taken into account in the derivation of the sea surface reflectance. In other works, the errors originating from neglecting polarization were shown at the top-of-atmosphere level [31,41]. The results of these studies showed similar dependencies of the errors on the viewing geometry as in Fig. 3(c), which corroborates that those errors stem from the polarization effects occurring at the air-sea interface.

A synoptic view of the impact of atmospheric polarization on the sea surface reflectance can be obtained by plotting the relative difference $\Delta\rho_{\text{surf}}$ for all the azimuth and solar angles, and for the viewing angle of 40° commonly used in above-water radiometry; see Fig. 4. In Fig. 4(a), calculations were done at 550 nm for an aerosol optical thickness of 0.1 and for flat sea surface. The results displayed in this figure correspond to the case previously shown in Fig. 3(c) but extended to all azimuth conditions. For instance, it can be seen in this figure that the relative difference at 90° azimuth is first negative for solar angles smaller than 35° and then becomes positive for greater solar angles. It can also be noted that the large negative differences occur in the vicinity of 40° solar angle and 0° azimuth. However, this region corresponds to the zone of influence of the sun glint and cannot be used for above-water radiometry purposes.

For wind speeds of 4 and 10 m s^{-1} [Figs. 4(b) and 4(c)], the sea surface ruffles and becomes a rough surface on which myriads of wave facets can reflect light coming from various directions of the sky region, thereby creating depolarization of the signal by beam superposition. As a result, it could be expected that the impact of sky-light polarization on surface reflection is smoothed away when wind speed increases. Interestingly, this behavior does occur, but the relative difference $\Delta\rho_{\text{surf}}$ remains significant

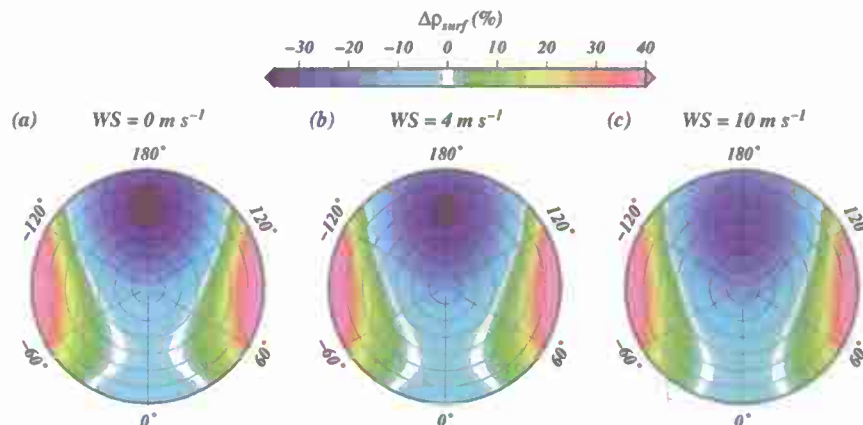


Fig. 4. (Color online) Relative difference $\Delta\rho_{\text{surf}}$ at 550 nm and an aerosol optical thickness of 0.1 for different wind speed conditions: (a) 0, (b) 4, and (c) 10 m s^{-1} . The polar diagrams account for all the azimuth and solar angles for a given viewing angle of 40° . The concentric circles represent the solar zenith angles by a step of 10° (from 0° to 70°), and angles in the polar diagrams represent the relative azimuth with the Sun.

over the viewing configurations. Based on this theoretical analysis, it can therefore be safely concluded that the polarization state of the sky light reflected on the sea surface must be accurately taken into account for estimating the sea surface reflectance and in turn the water-leaving radiance.

3. LISCO

A. LISCO Site

The LISCO platform is located at around 3 km from the shore of Long Island near Northport, New York, USA. The coordinates of the site are N 40°57'16", W 73°20'30". The bathymetry in the immediate vicinity of the platform exhibits a plateau at around 13 m depth. LISCO is located in the area of western Long Island Sound, which is usually moderately turbid, very productive, and principally driven by phytoplankton biomass and associated detrital materials rather than suspended sediments [42]. Steady surface currents in the LISCO area are around 0.3 m s^{-1} in average according to National Oceanic and Atmospheric Administration radar data sets. The instruments are positioned on a retractable tower on the platform with an elevation of 12 m.

B. Multispectral and Hyperspectral LISCO Data

The platform combines a multispectral SeaPRISM system (CIMEL Electronique, France) with a collocated hyperspectral HyperSAS system (Satlantic, Canada). The SeaPRISM system is part of AERONET and particularly of its ocean color (OC) component [4,8,23]. The instruments are positioned on a retractable tower on the LISCO platform with an elevation of 12 m. Both instruments were installed in October 2009 and have been providing data since then.

The SeaPRISM system is made up of CE-318 sun photometers modified to meet requirements for above-water radiometry. The photometers perform radiance measurements of the total radiance of the sea, $L_t(\theta_s, \theta_v, \phi)$, and the sky, $L_{\text{sky}}(\theta_s, \theta', \phi)$, for the relative azimuth angle with respect to the sun ϕ and the respective viewing angles θ_v and θ' , with $\theta_v = \pi - \theta'$. Thanks to the rotating feature of SeaPRISM, the azimuth ϕ is fixed to 90° regardless of the sun position; the downward zenith viewing angle θ_v is set to 40°. The spectral bands of the SeaPRISM system are centered on 413, 442, 491, 551, 668, 870, and 1018 nm.

The collocated hyperspectral measurements are made by a HyperSAS system, providing high-precision hyperspectral above-water measurements of downwelling and upwelling spectral radiances as well as downwelling spectral irradiance. The radiance and irradiance measurements of HyperSAS are carried out for 180 spectral channels regularly spaced between 305 and 905 nm. HyperSAS has two radiance sensors, one looking down at the water and the other looking skywards. These sensors provide the sea $L_t(\lambda, \theta, \phi)$ and the sky radiance $L_{\text{sky}}(\lambda, \theta', \phi)$ for the same viewing angle as SeaPRISM, that is, $\theta_v = 40^\circ$.

However, the sensors are pointing exactly westwards, resulting in a relative azimuth ϕ changing with respect to the sun position. Each HyperSAS and SeaPRISM sea-viewing measurement sequence is executed every 30 min within plus or minus 4 h of 12:00 local time (LT).

The calibration of the SeaPRISM sun photometer was carried out by the NASA AERONET group in accordance with the standard procedures of AERONET-OC. The HyperSAS system calibration was carried out by Satlantic, Inc. (Halifax, Canada), and checked at the City College of New York (CCNY) Optical Remote Sensing Lab. The recalibration by Satlantic, Inc., of the HyperSAS system has shown a radiometric stability, over a time period of approximately 15 months, of better than 1% for up- and downwelling radiance sensors and better than 0.5% for the irradiance sensor. In addition, errors due to nonperfect cosine response of the irradiance sensor were estimated to be smaller than 2% on average. SeaPRISM data are transferred by a satellite link to NASA, processed by the NASA AERONET group, and posted on the NASA AERONET website. The near-real-time transmission of HyperSAS data is achieved by broadband cellular service to the CCNY server.

In this study, the SeaPRISM data used corresponds to the Level 2.0 data archive. Those data are cloud screened and quality assured, with up-to-date calibration. The HyperSAS data used corresponds to data which have successfully passed the data-quality check as defined in [9].

C. Aerosol Retrievals

In addition to these OC measurements, the regular data acquisitions of AERONET are also carried out, which permits accurate retrievals of the aerosol optical thickness and the fine-coarse aerosol mode fraction [43,44]. The aerosol component of AERONET [23,45] is a well-established network of over 200 semi-permanent ground-based sunphotometers worldwide. They provide standardized high quality aerosol measurements which are used here as reference data. Visible and near-infrared measurements of the aerosol optical depth are available with an accuracy of about 0.01 to 0.02. The LISCO Level 2.0 data archive of aerosol inversion is used in this study with, specifically, the respective spectral aerosol optical thicknesses of the fine- and coarse-mode aerosols as derived by the spectral deconvolution method of [44].

4. Retrieval of Water-Leaving Radiance from Above-Water Measurements

A. Modeling of the Sky Glint Contribution

The aerosols are assumed to follow a bimodal size distribution. As pointed out by Whitby [46] and Junge [47,48], a realistic size distribution can be modeled based on the sum of single modes. Several studies showed that a satisfactory simulation of aerosols can be obtained using a mixture of a fine mode

with a coarse mode [49–53]. The size distribution $N(r)$ of these two modes can be parameterized with the same log-normal expression, as follows:

$$dN(r) = \frac{1}{\sigma\sqrt{2\pi}} \exp\left[-\frac{1}{2}\left(\frac{\log r - \log \bar{r}}{\sigma}\right)^2\right] d \log r, \quad (15)$$

where \bar{r} , the mean radius, and σ , the standard deviation of $\log r$, are specific of a given aerosol mode. Based on this log-normal size distribution, the optical properties of these two aerosol models were computed through Mie theory calculation assuming spherical particles. The microphysical properties were chosen to be as close as possible to the AERONET inversion data typically retrieved at the LISCO site. The fine mode corresponds to a mean radius of 0.17 μm , a refractive index of 1.45, and a standard deviation of the size distribution of 0.46. The coarse mode corresponds to a mean radius of 2.0 μm , a refractive index of 1.35, and a standard deviation of the size distribution of 0.75. The fine-mode aerosol model is assumed to be slightly absorbing accordingly to the AERONET retrievals [11] with an imaginary part of the refractive index equal to 0.005.

Based on the respective microphysical properties of the fine- and coarse-mode aerosols, the sea surface reflectance ρ_{surf} was computed through radiative transfer computation including polarization effects as discussed in Section 2. This reflectance was computed for the fine mode and coarse mode, separately, for aerosol optical thicknesses τ_a ranging from 0 to 0.4 by a step of 0.05. The radiative transfer computations were carried out for viewing and solar zenith angles ranging from 2° to 90° with increments of around 1.5°. The sea surface reflectance is exactly recomposed for any azimuth angle based on a Fourier series approach. Then, the total sea surface reflectance of the fine and coarse aerosol mixture is computed, as shown by Wang and Gordon [54], for any viewing configuration defined by $(\theta_s, \theta_v, \phi)$:

$$\rho_{\text{surf}}(\tau_a(\lambda); \theta_s, \theta_v, \phi) = \gamma \rho_{\text{surf}}^f(\tau_a(\lambda); \theta_s, \theta_v, \phi) + (1 - \gamma) \rho_{\text{surf}}^c(\tau_a(\lambda); \theta_s, \theta_v, \phi), \quad (16)$$

where ρ_{surf}^f and ρ_{surf}^c stand for the sea surface reflectance calculated for the fine mode and the coarse mode, respectively. They are calculated for any aerosol optical thickness by linear interpolation within the exact simulation generated for discrete τ_a values. The term γ is the mixing coefficient between the two aerosol modes (i.e., fine and coarse mode) given by

$$\gamma = \frac{\tau_a^f(\lambda)}{\tau_a(\lambda)}. \quad (17)$$

It is worth mentioning that Eq. (16) fails to accurately represent the Stokes vector of aerosol mixtures when strongly absorbing aerosols are present.

However, such an equation is frequently used in OC and aerosol remote sensing [55,56] because it permits introduction of a continuous variable, namely the mixing coefficient γ , thereby enhancing the representativeness of the aerosol models used in that scheme.

The total sea surface reflectance is then computed for the HyperSAS or SeaPRISM viewing configuration and for the coincident aerosol optical properties data derived from the collocated AERONET system. The determination of the aerosol mixture is based on the Level 2.0 AERONET inversion data products acquired within a time window of plus or minus 20 min of the acquisition sequence considered. Finally, based on Eqs. (13) and (16), the water-leaving radiance is retrieved from the measured total radiance L_t as follows:

$$L_w(\theta_s, \theta_v, \phi) = L_t^*(\theta_s, \theta_v, \phi) - \frac{\rho_{\text{surf}}(\theta_s, \theta_v, \phi) E_s(\theta_s)}{\pi}. \quad (18)$$

B. Normalized Water-Leaving Radiance

The exact normalized water-leaving radiance, L_{WN} , is then obtained from $L_w(\lambda, \theta, \varphi)$ as follows:

$$L_{WN} = C_{\text{RQ}}(\theta_s, \theta_v, \phi, \tau_a, \text{IOP}, \text{ws}) C_{f/Q}(\theta_s, \tau_a, \text{IOP}) \times \frac{L_w(\theta_s, \theta_v, \phi)}{E_s(\theta_s)} \bar{F}_0. \quad (19)$$

where τ_a and IOP stand for the aerosol optical thickness and the inherent optical properties, respectively. C_{RQ} and $C_{f/Q}$ are introduced to remove the dependence from the viewing geometry due to the refraction of wavy sea surface and the bidirectional effects in L_w , respectively; the exact formulations of these terms can be found in [4] for example. The term \bar{F}_0 is the theoretical spectral extraterrestrial solar irradiance for the mean Sun–Earth distance [57]. E_s is downwelling spectral irradiance just above the sea surface.

In order to apply the correction scheme described in the previous section, the spectral values of E_s are needed. The value of E_s is directly measured by the irradiance sensor of the HyperSAS system. In contrast, the SeaPRISM system does not have an irradiance radiometer, and E_s is accordingly parameterized in the official SeaPRISM processing as follows:

$$E_s(\theta_s) = T_{\text{tot}}(\theta_s) \cos(\theta_s) D^2 \bar{F}_0, \quad (20)$$

where D^2 accounts for the variation of the Sun–Earth distance with the day of the year [58]; T_{tot} stands for the total atmospheric irradiance transmittance, which is the sum of its direct and diffuse components. In the NASA SeaPRISM processing, the latter is computed at a given wavelength λ following the empirical relationship [59,60]

$$T_{\text{tot_SeaPRISM}}(\lambda, \theta_s) = \exp\left(-\frac{[0.5\tau_r(\lambda) + C_a\tau_a(\lambda) + \tau_{O3}(\lambda)]}{\cos\theta_0}\right), \quad (21)$$

where τ_r , τ_a , and τ_{O3} are the Rayleigh, aerosol and ozone optical thicknesses, respectively. The C_a coefficient accounts for aerosol phase function and absorption properties, and its value is typically around 0.14 with a slight spectral dependence. In the SeaPRISM processing, τ_r is computed taking into account the atmospheric pressure variations, τ_a is directly retrieved by the sun photometer component of the SeaPRISM measurements for each spectral band, and τ_{O3} is computed from the Total Ozone Mapping Spectrometer dataset. Note that the use of the parameterization of Eq. (21) might induce small discrepancies between the HyperSAS and SeaPRISM irradiance products for the usual atmospheric conditions of the LISCO site [9].

5. Application to LISCO Above-Water Measurements

In this section, the proposed algorithm for correction of the sky light reflection is evaluated on the basis of the 1.5-year LISCO dataset of multi- and hyperspectral measurements. Specifically, the consistency of the water-leaving radiance retrieved from the collocated instrumentation is analyzed and the implications of considering polarization are discussed.

A. SeaPRISM Data

The correction scheme, described in the previous section, was applied to the SeaPRISM Level 2.0 data over the 1.5-year period of LISCO acquisitions, which have been reprocessed by the AERONET program for Level 2.0 data production [4]. Those data were controlled to exclude any data prohibitively contaminated by sun glint, foam, clouds, or any other undesirable environmental effects. Thus, the new correction scheme and the standard one can be meaningfully compared to infer how well those schemes are handling reflection of the diffuse sky light of the rough sea surface.

The LISCO data were processed with the proposed algorithm following two modalities: first without considering polarization, that is to say, the correction was performed based on scalar radiative transfer computations. With this modality, the water-leaving radiances are retrieved for physical assumptions similar to those made within the NASA processing scheme. The second modality makes use of vector radiative transfer computations, enabling it to fully consider the polarization state of the signal during the sky-light correction step. The respective time series of exact normalized water-leaving radiances retrieved by the standard and the new correction scheme with and without polarization consideration are shown in Fig. 5. In general, for all the spectral bands except that centered on 413 nm, the seasonal variations observed on the three datasets are consistent over the whole 1.5-year period. Especially, the distinctive peak of radiance occurring after March 17, 2010, resulting from an increase of sediment

concentration following a significant storm event with higher riverine input and water body mixing, can be observed in Fig. 5. Moreover, the NASA processing and the proposed algorithm yield very similar water-leaving radiance retrievals when polarization is ignored. As a result, it can be concluded that the seasonal changes are captured well by the two correction schemes over the 1.5-year datasets of LISCO acquisitions.

At the longer wavelengths, namely between 491 and 668 nm, the two modalities (with and without polarization) yield virtually similar results with the exception of the winter periods, where slight differences can be seen (green and red dots are not superimposed in Fig. 5). At this period of the year, the Sun remains low on the horizon within daytime. The amount of diffuse sky light is therefore high in comparison to direct sunlight. In addition, it can be remembered that the nondiagonal terms of the Fresnel matrix (i.e., R_{12} and R_{13}) exhibit, for large solar angles, values practically as large as those of the R_{11} term (see Fig. 2), which is usually used for sky light reflection calculations in the standard correction scheme. As a result, the discrepancies between the standard and the new polarization-based correction scheme are enhanced for large solar zenith angles, and, therefore, the differences between the retrieved water-leaving radiances are more pronounced during winter time.

At the shorter wavelengths, the optical thickness of the air molecules is much higher than at longer wavelengths. This optical behavior of the atmosphere makes the diffuse skylight more intense and polarized toward the shorter wavelengths. It can be readily seen in Fig. 5(a) that the higher degree of polarization occurring at 413 nm, for instance, induces strong discrepancies between retrievals when polarization is taken into account or not. Moreover, these discrepancies are also enhanced in winter, as discussed before, producing very large differences between the two correction schemes.

This qualitative view offered by the times series enables us to conclude that the polarization of diffuse sky light significantly impacts the water-leaving retrieval from above-water radiometric measurements at the shortest wavelengths. On the other hand, a more quantitative view on polarization impacts can be reached by matchup comparison of the coincident products obtained through application of the two different correction schemes. In order to analyze these comparisons the following statistical indicators are used. The unbiased relative percent difference (URPD) and the absolute unbiased relative percent difference (|URPD|) are defined similarly to [7,38]:

$$\text{URPD} = 200 \times \frac{1}{N} \sum_{i=1}^N \frac{y_i - x_i}{x_i + y_i}, \quad (22)$$

$$|\text{URPD}| = 200 \times \frac{1}{N} \sum_{i=1}^N \left| \frac{y_i - x_i}{x_i + y_i} \right|, \quad (23)$$

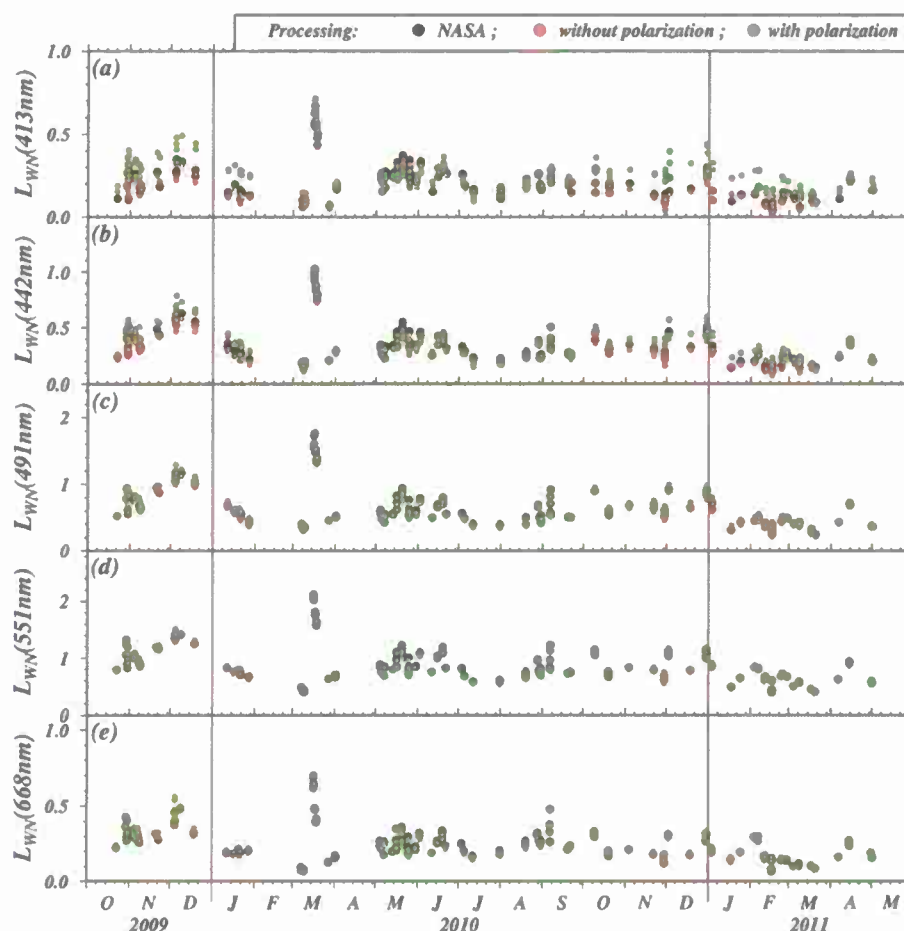


Fig. 5. (Color online) Time series of the normalized water-leaving radiances (in $\text{mW cm}^{-2} \text{sr}^{-1} \mu\text{m}^{-1}$) obtained from the LISCO SeaPRISM Level 2.0 data by the NASA algorithm (black dots) and the radiative-transfer-based algorithm without (red dots) and with polarization (green dots) at (a) 413, (b) 442, (c) 491, (d) 551, and (e) 668 nm.

where x stands for the standard products and y for the new product to be evaluated. N is the number of matchup points. The root-mean-square differences (RMSD) complete those statistical indicators. Finally, a least squares fit is also adjusted within the matchup points, with the associated coefficient of determination, R^2 , and the equation of the regression line. It should be noted that no statistical filtering has been applied to the following comparisons to remove outliers.

The matchup comparison of the normalized water-leaving radiances obtained from Level 2.0 SeaPRISM data by the standard and new correction schemes when polarization is ignored is shown in Fig. 6(a) for the spectral bands of interest. To complete this spectral average view, a summary of the statistical indicators calculated for each spectral band is provided in Table 1. In this comparison, the two datasets were built while neglecting polarization impacts in the respective data processing. In this sense, the comparison of Fig. 6(a) enables us to validate the proposed algorithm based on radiative transfer computation and aerosol knowledge because both procedures rely on the same physical assumptions. On the spectral average, the coefficient of determination R^2 is

almost 1, showing a perfect correlation with a regression line very close to the 1:1 line. This strong correlation is observed for every wavelength as shown by the spectral values of $R^2 > 0.95$ in Table 1. The overall dispersion is reasonably low with $|\text{URPD}| < 5\%$ and an RMSD of $0.021 \text{ mW cm}^{-2} \text{sr}^{-1} \mu\text{m}^{-1}$. This excellent agreement between the two datasets demonstrates the correctness and reliability of the proposed radiative-transfer-based approach for correcting the reflected sea surface signal.

Because the radiative-transfer-based approach has been validated over the whole time series, the proposed algorithm can be used to analyze the impact of polarization on the water-leaving radiance retrieval. Figure 6(b) shows the comparison of the exact water-leaving radiances obtained with the proposed algorithm when polarization is neglected or fully considered. On the spectral average, the coefficient of determination R^2 is 0.99, showing a very strong correlation between retrievals. However, this parameter R^2 decreases rapidly at the shorter wavelengths. At 551 nm, R^2 is equal to 0.99 and decreases down to 0.81 at 413 nm. At the same time, the $|\text{URPD}|$ values increases from 1.7% to 15.3% between 551 and 413 nm for a spectral average of 6.5%. Therefore, it

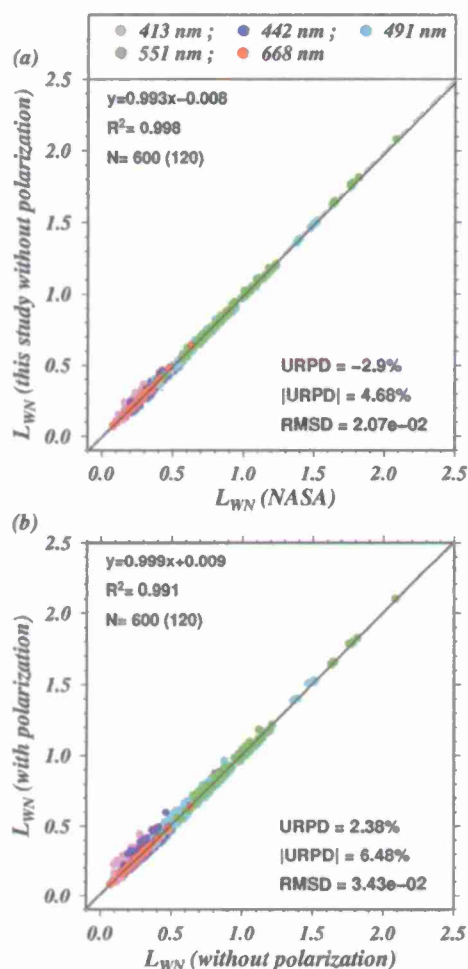


Fig. 6. (Color online) Comparison of the exact normalized water-leaving radiances (in $\text{mW cm}^{-2} \text{sr}^{-1} \mu\text{m}^{-1}$) derived from SeaPRISM measurements through (a) the standard data processing and the radiative-transfer-based correction scheme ignoring polarization and (b) the radiative-transfer-based correction modality ignoring polarization and that fully considering the polarization impacts.

can be concluded that the impact of polarization on sky-light reflection is conspicuous at the shorter wavelengths and is markedly less prohibitive in the green and red part of the spectrum. On the other hand, it is worth noticing that the URPD, $|\text{URPD}|$, and RMSD values are in general larger than those

observed in Fig. 6(a) and are quite comparable to those retrieved in the matchup comparison between above- and in-water measurements [10,15,38], proving that the polarization effects related to sky-light reflection is of major importance when dealing with water-leaving radiance retrieval from above water.

B. HyperSAS Data

In the same manner as for SeaPRISM data, the standard and new sea surface-correction schemes were applied to the HyperSAS measurements to retrieve the exact normalized water-leaving radiance, L_{WN} . However, the setup of the HyperSAS system is noticeably different than that of SeaPRISM as the HyperSAS radiometers are fixed on the platform, and their relative azimuth with the Sun is perpetually changing over the day. In order to illustrate the efficiency of the respective standard and new correction schemes, the spectra of L_{WN} retrieved within a day are displayed in Fig. 7. On August 19, 2010, a field cruise was conducted in the vicinity of the LISCO platform, enabling us to check the clear sky and low wind conditions of that day, which was chosen for the illustration of Fig. 7.

The L_{WN} spectra estimated by the standard correction scheme are plotted in Fig. 7(a) for the different relative azimuths for which the HyperSAS measurements were performed. It can be readily seen in this figure that the azimuth variation induces slight variation of the retrieved L_{WN} provided that the azimuth is larger than 70° for wavelengths longer than 440 nm, approximately. It should be noted that the quality check procedure of LISCO data, recently defined on the basis of the standard correction scheme [9], recommended utilization of HyperSAS L_{WN} only if measurements were performed for azimuths larger than 70° . Nevertheless, the spectrum retrieved from measurements performed with an azimuth of 73° shows significant departure from the spectra retrieved for larger azimuth, whereas it would probably be expected to measure a virtually unchanged spectrum within the same day of interest. Furthermore, when the azimuth is 59° , the standard correction fails to retrieve physically meaningful water-leaving radiance as demonstrated by the negative values obtained for wavelengths smaller than

Table 1. Summary of the Statistical Indicators for the Comparison of the Exact Normalized Water-Leaving Radiances of Fig. 6

Data		Wavelength (nm)					All Wavelengths
		413	442	491	551	668	
Figure 6(a)	R^2	0.951	0.987	0.997	0.999	0.996	0.998
	Regression line	$0.96x + 0.01$	$0.99x - 0.01$	$1.00x - 0.02$	$1.01x - 0.02$	$1.01x - 0.01$	$0.99x - 0.01$
	URPD	-0.8	-5.4	-2.7	-1.8	-3.6	-2.9
	$ \text{URPD} $	7.6	6.8	3.2	1.9	3.8	4.7
	RMSD	2.37×10^{-2}	2.60×10^{-2}	2.16×10^{-2}	1.83×10^{-2}	1.04×10^{-2}	2.07×10^{-2}
Figure 6(b)	R^2	0.811	0.943	0.989	0.996	0.991	0.991
	Regression line	$0.95x + 0.03$	$1.02x - 0.01$	$1.02x + 0.00$	$1.01x + 0.00$	$1.01x + 0.00$	$1.00x + 0.01$
	URPD	6.3	3.1	1.0	0.5	0.9	2.4
	$ \text{URPD} $	15.3	9.1	3.6	1.7	2.8	6.5
	RMSD	5.11×10^{-2}	4.30×10^{-2}	3.05×10^{-2}	2.06×10^{-2}	0.88×10^{-2}	3.43×10^{-2}

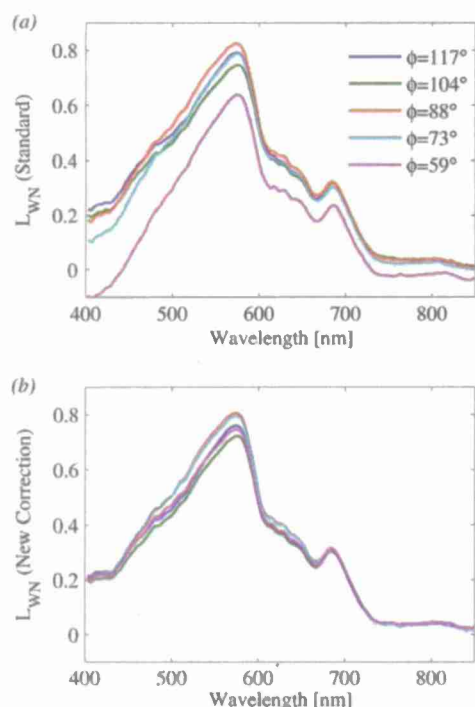


Fig. 7. (Color online) Exact water-leaving radiance spectra (in $\text{mW cm}^{-2} \text{sr}^{-1} \mu\text{m}^{-1}$) retrieved through (a) the standard and (b) the new polarization-based correction scheme applied to the HyperSAS data of August 19, 2010. The colors indicate the different relative azimuths ϕ for which measurements were performed.

450 nm and longer than 740 nm. Therefore, the L_{WN} values retrieved by the standard correction scheme are characterized by significant azimuth dependence even though the measurement conditions were satisfactory (e.g., low wind speed, clear sky).

In contrast, application of the new correction scheme on the same dataset yields very similar spectra over same the day regardless of the azimuth of the acquisitions; see Fig. 7(b). In addition, the slight variations observed for the intermediate wavelengths (e.g., 490–630 nm) are most likely connected to biological changes induced by irradiance variation over the day. Regarding the infrared part of the spectrum where the optical impact of phytoplankton is negligible, the retrieved L_{WN} are markedly constant for all the azimuths considered. The same observation is true for the shorter wavelengths. Based on the remarkable consistency of those HyperSAS spectra within the same day, it can be safely concluded that the new correction scheme yields meaningful L_{WN} estimations, thereby validating the polarization-based approach.

As for SeaPRISM data, matchup comparisons between L_{WN} retrieved by the standard and new correction schemes applied to HyperSAS data were performed over the 1.5-year dataset. Figure 8(a) shows the comparison between the standard data processing and the radiative-transfer-based correction scheme ignoring polarization, whereas Fig. 8(b) shows the comparison between the radiative-transfer-based correction modality ignoring polarization and

that fully considering the polarization impacts. The statistical indicators are summarized in Table 2. In those comparisons, the azimuth range was restricted to 70° – 180° because the HyperSAS retrievals are quality assured outside this range for the standard correction scheme.

The comparison of the normalized water-leaving radiances obtained from HyperSAS data by the standard and new correction schemes when polarization is ignored is shown in Fig. 8(a). In this comparison, the two datasets were built neglecting polarization impacts in the respective data processing. This comparison exhibits very similar results to those of Fig. 6(a) based on the SeaPRISM datasets. On spectral average, the coefficient of determination R^2 is almost 1, showing a perfect correlation with a regression line very close to the 1:1 line. This strong correlation is observed for every wavelength as shown by the spectral values of $R^2 > 0.97$ in Table 2. The overall dispersion is reasonably low with $|\text{URPD}| < 5\%$ and an RMSD of $0.026 \text{ mW cm}^{-2} \text{sr}^{-1} \mu\text{m}^{-1}$. Once again, this excellent agreement between the two datasets

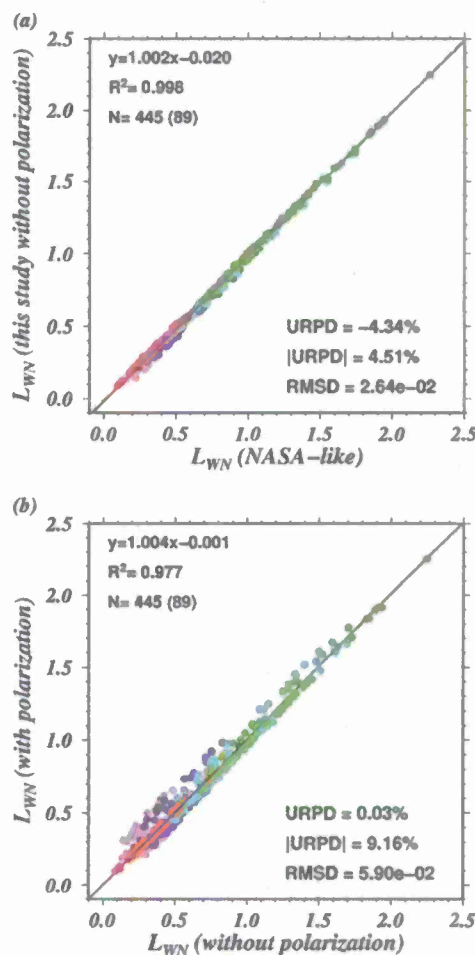


Fig. 8. (Color online) Comparison of the exact normalized water-leaving radiances (in $\text{mW cm}^{-2} \text{sr}^{-1} \mu\text{m}^{-1}$) derived from HyperSAS measurements through the standard data processing and the polarization-based correction scheme. The azimuth range is between 70° and 180° .

Table 2. Summary of the Statistical Indicators for the Comparison of the Exact Normalized Water-Leaving Radiances of Fig. 8

Data		Wavelength (nm)					All Wavelengths
		413	442	491	551	668	
Figure 8(a)	R^2	0.971	0.990	0.998	0.999	0.996	0.998
	Regression line	$0.99x - 0.03$	$0.99x - 0.02$	$1.00x - 0.02$	$1.01x - 0.01$	$1.01x - 0.01$	$1.00x - 0.02$
	URPD	-9.2	-6.5	-2.8	-1.2	-1.8	-4.3
	URPD	9.3	6.6	2.8	1.4	2.4	4.5
	RMSD	3.53×10^{-2}	3.51×10^{-2}	2.58×10^{-2}	1.66×10^{-2}	0.85×10^{-2}	2.64×10^{-2}
Figure 8(b)	R^2	0.580	0.865	0.976	0.990	0.985	0.977
	Regression line	$0.81x + 0.07$	$1.02x - 0.01$	$1.04x - 0.03$	$1.01x - 0.01$	$1.02x - 0.01$	$1.00x + 0.00$
	URPD	1.2	-0.5	-0.5	0.0	-0.1	0.0
	URPD	20.6	12.8	5.5	2.8	4.0	9.2
	RMSD	8.53×10^{-2}	7.56×10^{-2}	5.45×10^{-2}	3.49×10^{-2}	1.45×10^{-2}	5.90×10^{-2}

corroborates the correctness and reliability of the proposed radiative-transfer-based approach already demonstrated based on the SeaPRISM datasets.

Conversely, the comparison between the datasets generated in neglecting or accounting for polarization exhibits more pronounced discrepancies in Fig. 8(b). On the spectral average, the coefficient of determination of 0.98 shows a good correlation, but the averaged |URPD| value of about 9% and an RMSD equal to $0.059 \text{ mW cm}^{-2} \text{ sr}^{-1} \mu\text{m}^{-1}$ indicate significant dispersion induced by the polarization effects. Moreover, a strong spectral dependence is also observed with increasing |URPD| values toward the shorter wavelengths, namely 2.8% at 551 nm and 20% at 413 nm, accompanied by a decrease of R^2 from 0.99 to 0.58. It is worth noticing that all those observed discrepancies generated by the polarization state of the reflected sky light are generally more pronounced for the HyperSAS datasets than for the SeaPRISM ones. This can be explained by the different geometric setups used by the two systems: SeaPRISM acquisitions are performed for a fixed relative azimuth angle of 90° whereas HyperSAS data are acquired for various relative azimuth angles, here comprising those between 70° and 180° . As discussed in Section 2.C (see Fig. 4), the polarization effects on the sea surface signal are highly variable with azimuth. In addition, acquisitions at small relative azimuths are more impacted by the sky-light reflection because the diffuse sky is generally increasing when the sensor is pointing closer to the solar plane. In conclusion, the polarization effects should be accounted for when correcting above-water measurements for the sea surface signal (impact larger than 9% on the water-leaving radiance retrievals) and particularly when dealing with a large range of azimuth angles as is the case for the HyperSAS system at the LISCO site or other radiometers commonly in use in oceanographic field cruises.

The implication of considering polarization for sea surface-reflectance estimation can then be evaluated on the basis of comparison of the collocated and coincident SeaPRISM and HyperSAS datasets. In this case, comparisons between SeaPRISM and HyperSAS L_{WN} retrievals were carried out for the five main SeaPRISM spectral bands, namely 413, 442, 491, 551, and 668 nm. The hyperspectral

HyperSAS data were integrated with the sensor relative spectral response function of each SeaPRISM band in order to produce equivalent data for both systems. The data involved were restricted to SeaPRISM measurement sequences taken within ± 10 min of HyperSAS sequence intervals. Because the sequence interval is 30 min for both systems, the comparisons were always achieved between the same single sequences.

In order to properly examine the consistency of the SeaPRISM and HyperSAS datasets, the two datasets were normalized by the same downwelling irradiance values measured by the HyperSAS irradiance sensor. In the comparisons, the azimuth range of the HyperSAS acquisitions was first considered between 70° and 180° , corresponding to the good data quality of the HyperSAS standard processing. The potential improvements of the new correction scheme for supplementary azimuth range, namely azimuth angles down to 30° , were then investigated. Results of these comparisons are displayed in Fig. 9 for different modalities of the water-leaving radiance retrieval algorithm, and statistical indicators are summarized in Table 3.

In Fig. 9(a), the L_{WN} retrieved by the standard correction scheme applied to SeaPRISM and HyperSAS data are compared for HyperSAS azimuth angles occurring between 70° and 180° . Notwithstanding the strong correlation ($R^2 = 0.98$), the comparison shows significant dispersion with |URPD| = 13.5% and $\text{RMSD} = 0.078 \text{ mW cm}^{-2} \text{ sr}^{-1} \mu\text{m}^{-1}$ on spectral average. At 413 nm, where polarization impact is the strongest, the respective datasets are less correlated ($R^2 = 0.81$) and exhibit important dispersions between each other (|URPD| = 24.6%; $\text{RMSD} = 0.092 \text{ mW cm}^{-2} \text{ sr}^{-1} \mu\text{m}^{-1}$). In contrast, when comparisons are performed based on the new-correction-scheme retrievals (Fig. 9(b)), the overall correlation is stronger with $R^2 = 0.98$ for a |URPD| value around 9.9%. This is particularly true at 413 nm where $R^2 = 0.91$ for a |URPD| value of 12% and a low RMSD of $0.046 \text{ mW cm}^{-2} \text{ sr}^{-1} \mu\text{m}^{-1}$. These values are in the same order of magnitude as other studies examining comparison of in-water and above-water datasets; see [10] for example. Thus the new correction scheme enables us to reconcile the two datasets

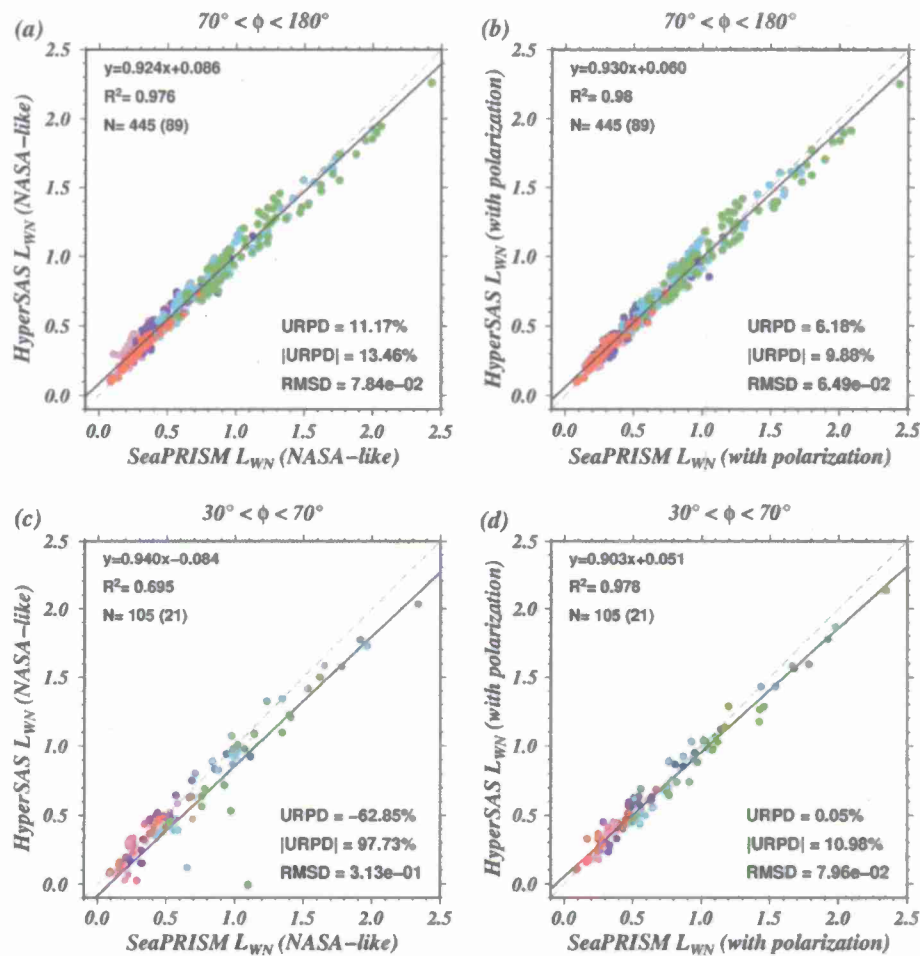


Fig. 9. (Color online) Comparison of the exact normalized water-leaving radiances (in $\text{mW cm}^{-2} \text{sr}^{-1} \mu\text{m}^{-1}$) derived from HYPERAS and SeaPRISM measurements through (a), (c) the standard data processing and (b), (d) the radiative-transfer-based correction scheme. The azimuth range of HyperSAS data acquisition is comprised (a), (b) between 70° and 180° and (c), (d) between 30° and 70° .

Table 3. Summary of the Statistical Indicators for the Comparison of the Exact Normalized Water-Leaving Radiances of Fig. 9

Data		Wavelength (nm)					All Wavelengths
		413	442	491	551	668	
Figure 9(a)	R^2	0.812	0.921	0.966	0.954	0.953	0.976
	Regression line	$0.98x + 0.08$	$0.94x + 0.10$	$0.92x + 0.10$	$0.89x + 0.11$	$0.95x + 0.04$	$0.92x + 0.09$
	URPD	23.8	14.5	5.9	0.4	11.1	11.2
	$ URPD $	24.6	15.8	8.4	6.9	11.6	13.5
	RMSD	9.21×10^{-2}	8.43×10^{-2}	7.70×10^{-2}	8.74×10^{-2}	3.97×10^{-2}	7.84×10^{-2}
Figure 9(b)	R^2	0.910	0.944	0.970	0.954	0.941	0.980
	Regression line	$0.92x + 0.04$	$0.91x + 0.07$	$0.92x + 0.08$	$0.88x + 0.11$	$0.94x + 0.04$	$0.93x + 0.06$
	URPD	8.0	8.2	3.5	-0.3	11.4	6.2
	$ URPD $	12.0	10.9	7.1	7.0	12.2	9.9
	RMSD	4.61×10^{-2}	6.16×10^{-2}	7.05×10^{-2}	8.15×10^{-2}	4.25×10^{-2}	6.49×10^{-2}
Figure 9(c)	R^2	0.086	0.335	0.755	0.778	0.403	0.695
	Regression line	$0.81x - 0.08$	$1.05x - 0.14$	$1.04x - 0.16$	$0.93x + 0.10$	$1.07x + 0.06$	$0.94x - 0.08$
	URPD	-262.7	-13.1	-36.3	-23.5	20.9	-62.8
	$ URPD $	305.6	69.9	39.1	23.7	50.3	97.7
	RMSD	4.00×10^{-1}	3.64×10^{-1}	2.73×10^{-1}	2.96×10^{-1}	1.87×10^{-1}	3.13×10^{-1}
Figure 9(d)	R^2	0.905	0.931	0.970	0.970	0.910	0.976
	Regression line	$1.01x - 0.01$	$0.99x + 0.03$	$0.95x + 0.02$	$0.89x + 0.08$	$0.97x + 0.04$	$0.90x + 0.06$
	URPD	-2.7	2.8	-3.5	-7.2	10.9	0.1
	$ URPD $	12.1	11.3	8.6	10.1	12.6	11.0
	RMSD	4.59×10^{-2}	6.64×10^{-2}	6.55×10^{-2}	1.27×10^{-1}	5.45×10^{-2}	7.96×10^{-2}

over the whole spectral range. It can therefore be safely concluded that polarization effects on diffuse sky-light reflection on the sea surface must be considered for accurate derivation of the water-leaving radiance from above water.

In Figs. 9(c) and 9(d), the L_{WN} retrieved by the standard and new correction schemes are compared for HyperSAS azimuth angles comprising between 30° and 70°. It was already noted elsewhere that azimuths smaller than 70° might lead to very low data quality when the standard processing is applied [9]. This behavior can be readily observed in Fig. 9(c), where correlation between the SeaPRISM data (acquired for a 90° azimuth angle) and the HyperSAS data (acquired for azimuths ranging from 30° to 70°) is markedly low ($R^2 = 0.69$), associated with a prohibitive dispersion ($|URPD| \sim 98\%$) due to inaccurate correction for sea surface signal in the HyperSAS data processing. In contrast, the polarization-based processing applied to the same raw data yields successful retrievals for the same azimuth range. Figure 9(d) shows strong correlation ($R^2 = 0.98$) associated with satisfactory dispersion ($|URPD| < 11\%$), similarly to the results obtained for the previous azimuth range of [70°, 180°]. This provides strong evidence that one of the main limiting factors for water-leaving derivation for small azimuth angles arises from ignoring the polarization component of the sea surface signal in above-water data processing. Therefore, it is advisable to account for polarization in data processing of above-water measurements when the azimuth range is restricted to small angles as can happen in field experiments (e.g., due to ship shadow avoidance). To conclude, the spectral consistency of the HyperSAS data over the day and the reconciliation of HyperSAS and SeaPRISM datasets, thanks to the polarization-based correction scheme, demonstrates the utility and validity of considering the whole physical phenomenon (intensity plus polarization of light) of sky-light reflection on a rough sea surface.

6. Conclusion and Perspectives

The water-leaving radiation measured from the above-water level is strongly affected by the effect of the sky-light reflection on the ruffled sea surface. This contamination might be sometimes prohibitive for accurate measurement of the water-leaving radiance. Fortunately, retrievals of the water-leaving radiance can be achieved in most cases provided that sun and sky glint have been accurately handled and subtracted from the total signal. In this study, the estimation of the sea surface reflectance originating from sky-light reflection has been investigated on the basis of the full-ocean-surface Fresnel matrix, which includes reflection of the polarization terms of light radiance.

The sensitivity of above-water measurements to the polarization state of the incident sky light has been theoretically analyzed based on radiative transfer computation. It has been shown that polarization

of incident light on the sea surface induces significant variations of the upwelling radiance field. In particular, the reflectance of the sea surface is strongly dependent on the polarization state of the downwelling sky light, which is mostly driven by the relative proportions of air molecules and aerosols. In addition, the sea state must be accurately handled to express the polarization contribution to the surface reflectance. It was also shown that errors in the surface reflectance estimation can reach more than 50% for viewing geometries generally used in above-water radiometry.

A newly developed correction scheme for sky-light reflection has been described and evaluated based on the data acquired over 1.5 years at LISCO, which combines an AERONET SeaPRISM system with a hyperspectral HyperSAS system. In this scheme, the aerosol properties retrieved by the standard inversion algorithm of the AERONET system are used to simulate the sea surface reflectance by including polarization in the resolution of the radiative transfer equation. Thus, the surface reflectance is retrieved for each multi- or hyperspectral measurement acquired from the LISCO platform. The normalized water-leaving radiance L_{WN} was then derived after subtraction of the sea surface component of the measured signal.

The validity and reliability of the proposed radiative-transfer-based approach for correcting the sea surface reflected signal has been confirmed based on comparison of the Level 2 AERONET-OC data with the outputs of the proposed algorithm when polarization is ignored (i.e., $R^2 > 0.99$ and $|URPD| < 5\%$). On the other hand, it has been demonstrated that the L_{WN} retrieved values are strongly affected when polarization information is taken into account. The multispectral SeaPRISM data are changed by 6.4% and 9.2% for the spectral average of the SeaPRISM and HyperSAS system, respectively. This change is greater than 15% at 413 nm where the sky is especially bright. Generally, a stronger impact of the polarization effects is observed for the hyperspectral HyperSAS data because of the fact that HyperSAS measurements are performed for variable azimuths during the course of the day. Furthermore, the quality of the HyperSAS data was greatly improved, especially for relative azimuths smaller than 70°, which enabled us to expand the time window of satisfactory HyperSAS measurements within a day.

The collocated SeaPRISM and HyperSAS L_{WN} datasets showed satisfactory agreement with each other when polarization was accounted for by the correction scheme, whereas significant discrepancies occur when polarization was neglected. In particular, the relative differences between the two datasets are now lower than 10% on spectral average for a wide range of azimuth angles. It was therefore concluded that the polarization effects arising during sky-light reflection on the sea surface significantly impact the water-leaving radiance derivation from above-water measurements and, in turn, the quality of the field

data utilized for satellite data validation or potential vicarious calibration purposes.

This polarization-based algorithm showed satisfactory performances for water-leaving radiance derivation at the LISCO site. However, it needs to be evaluated at other coastal sites exhibiting different optical characteristics, or even for above-water measurements performed on open ocean waters. In this manner, the relative impact of polarization on above-water radiometry might be quantified worldwide. In this case, the impact of the different types of aerosols should be first analyzed to generalize the approach. On the other hand, similar algorithms as that used in this study could be applied for processing radiometric datasets commonly acquired with HyperSAS-like systems during field cruise experiments where restriction in the possible viewing configurations might be a supplementary difficulty for accurate retrievals (e.g., ship shadow avoidance). Another way of improvement would be to reconsider the standard wave slope distribution used to model the roughness of the sea surface. In this direction, ongoing efforts are already undertaken to analyze and model wave dynamics at small time and spatial scales [61–64] which plays an important role on light reflection when dealing with small field of view and short time integration [65]. Nevertheless, and in every case, polarization effects at the surface will have to be accounted for.

This research was sponsored by NOAA and the Office of Naval Research. We would like to thank the NASA AERONET team for SeaPRISM calibration, data processing, and support of the site operations. The authors are grateful to two anonymous reviewers for their helpful comments.

References

1. International Ocean-Colour Coordinating Group, "Why ocean colour? The societal benefits of ocean-colour technology," in Reports of the International Ocean-Colour Coordinating Group, T. Platt, N. Hoepffner, V. Stuart, and C. Brown, eds. (International Ocean-Colour Coordinating Group, 2008), p. 7.
2. H. R. Gordon, "Atmospheric correction of ocean color imagery in the Earth observing system era," *J. Geophys. Res.* **102**, 17081–17106 (1997).
3. D. Antoine, F. d'Ortenzio, S. B. Hooker, G. Bécu, B. Gentili, D. Tailliez, and A. J. Scott, "Assessment of uncertainty in the ocean reflectance determined by three satellite ocean color sensors (MERIS, SeaWiFS and MODIS-A) at an offshore site in the Mediterranean Sea (BOUSSOLE project)," *J. Geophys. Res.* **113**, C07013 (2008).
4. G. Zibordi, B. N. Holben, I. Slutsker, D. Giles, D. D'Alimonte, F. Mélin, J. F. Berthon, D. Vandemark, H. Feng, G. Schuster, B. Fabbri, S. Kaitala, and J. Seppala, "AERONET-OC: a network for the validation of ocean color primary radiometric products," *J. Atmos. Ocean. Technol.* **26**, 1634–1651 (2009).
5. D. K. Clark, M. A. Yarbrough, M. E. Feinholz, S. Flora, W. Broenkow, Y. S. Kim, B. C. Johnson, S. W. Brown, M. Yuen, and J. L. Mueller, "MOBY, a radiometric buoy for performance monitoring and vicarious calibration of satellite ocean color sensors: measurement and data analysis protocols," *Ocean Optics Protocols for Satellite Ocean Color Sensor Validation, Revision 4*, 3–34 (2003).
6. J. L. Mueller, A. Morel, R. Frouin, C. Davis, R. Arnone, K. Carder, Z. P. Lee, R. G. Steward, S. Hooker, C. D. Mobley, S. McLean, B. Holben, M. Miller, C. Pietras, K. D. Knobelspiesse, G. S. Fargion, J. Porter, and K. Voss, *Ocean Optics Protocols for Satellite Ocean Color Sensor Validation, Revision 4, Volume III: Radiometric Measurements and Data Analysis Protocols*, J. L. Mueller, G. S. Fargion, and C. R. McClain, eds., NASA/TM-2003-211621 (NASA, 2003).
7. S. B. Hooker, G. Lazin, G. Zibordi, and S. McLean, "An evaluation of above-and in-water methods for determining water-leaving radiances," *J. Atmos. Ocean. Technol.* **19**, 486–515, (2002).
8. G. Zibordi, F. Mélin, S. B. Hooker, D. D'Alimonte, and B. Holben, "An autonomous above-water system for the validation of ocean color radiance data," *IEEE T. Geosci. Remote Sens.* **42**, 401–415 (2004).
9. T. Harmel, A. Gilerson, S. Hlaing, A. Tonizzo, T. Legbandt, A. Weidemann, R. Arnone, and S. Ahmed, "Long Island Sound Coastal Observatory: assessment of above-water radiometric measurement uncertainties using collocated multi and hyperspectral systems," *Appl. Opt.* **50**, 5842–5860 (2011).
10. G. Zibordi, "Comment on 'Long Island Sound Coastal Observatory: assessment of above-water radiometric measurement uncertainties using collocated multi and hyperspectral systems'," *Appl. Opt.* **51**, 3888–3892 (2012).
11. T. Harmel, A. Gilerson, S. Hlaing, A. Weidemann, R. Arnone, and S. Ahmed, "Long Island Sound Coastal Observatory: assessment of above-water radiometric measurement uncertainties using collocated multi and hyper-spectral systems: reply to comment," *Appl. Opt.* **51**, 3893–3899 (2012).
12. K. L. Carder and R. G. Steward, "A remote-sensing reflectance model of a red-tide dinoflagellate off west Florida," *Limnol. Oceanogr.* **30**, 286–298 (1985).
13. Z. Lee, K. L. Carder, R. G. Steward, T. G. Peacock, C. O. Davis, and J. L. Mueller, "Remote sensing reflectance and inherent optical properties of oceanic waters derived from above-water measurements," *Ocean Optics XIII*, 160–166 (1997).
14. C. D. Mobley, "Estimation of the remote-sensing reflectance from above-surface measurements," *Appl. Opt.* **38**, 7442–7455 (1999).
15. S. B. Hooker, G. Zibordi, J. F. Berthon, and J. W. Brown, "Above-water radiometry in shallow coastal waters," *Appl. Opt.* **43**, 4254–4268 (2004).
16. B. Fougnie, R. Frouin, P. Lecomte, and P. Y. Deschamps, "Reduction of skylight reflection effects in the above-water measurement of diffuse marine reflectance," *Appl. Opt.* **38**, 3844–3856 (1999).
17. Z. Lee, K. L. Carder, T. G. Peacock, and R. G. Steward, "Remote sensing reflectance measured with and without a vertical polarizer," *Proc. SPIE*, **2963**, 483–488 (1997).
18. P. Y. Deschamps, B. Fougnie, R. Frouin, P. Lecomte, and C. Verwaerde, "SIMBAD: a field radiometer for satellite ocean-color validation," *Appl. Opt.* **43**, 4055–4069 (2004).
19. G. Horvath, A. Barta, J. Gal, B. Suhai, and O. Haiman, "Ground-based full-sky imaging polarimetry of rapidly changing skies and its use for polarimetric cloud detection," *Appl. Opt.* **41**, 543–559 (2002).
20. A. Tonizzo, A. Gilerson, T. Harmel, A. Ibrahim, J. Chowdhary, B. Gross, F. Moshary, and S. Ahmed, "Estimating particle composition and size distribution from polarized water-leaving radiance," *Appl. Opt.* **50**, 5047–5058 (2011).
21. F. Waquet, B. Cairns, K. Knobelspiesse, J. Chowdhary, L. D. Travis, B. Schmid, and M. I. Mishchenko, "Polarimetric remote sensing of aerosols over land," *J. Geophys. Res.* **114**, D01206 (2009).
22. T. Harmel and M. Chami, "Influence of polarimetric satellite data measured in the visible region on aerosol detection and on the performance of atmospheric correction procedure over open ocean waters," *Opt. Express* **19**, 20960–20983 (2011).
23. B. N. Holben, T. F. Eck, I. Slutsker, D. Tanre, J. P. Buis, A. Setzer, E. Vermote, J. A. Reagan, Y. J. Kaufman, and T. Nakajima, "AERONET: a federated instrument network and data archive for aerosol characterization," *Remote Sens. Environ.* **66**, 1–16 (1998).
24. P. Koepke, "Effective reflectance of oceanic whitecaps," *Appl. Opt.* **23**, 1816–1824 (1984).
25. K. L. Coulson, *Polarization and Intensity of Light in the Atmosphere* (A. Deepak, 1988).

26. Y. Kawata, "Circular polarization of sunlight reflected by planetary atmospheres," *Icarus* **33**, 217–232 (1978).
27. S. Y. Kotchenova, E. F. Vermote, R. Matarrese, and F. J. Klemm, "Validation of a vector version of the 6S radiative transfer code for atmospheric correction of satellite data. Part I: path radiance," *Appl. Opt.* **45**, 6762–6774 (2006).
28. C. Cox and W. Munk, "Statistics of the sea surface derived from sun glitter," *J. Mar. Res.* **13**, 198–227 (1954).
29. C. Cox and W. Munk, "Measurement of the roughness of the sea surface from photographs of the suns glitter," *J. Opt. Soc. Am.* **44**, 838–850 (1954).
30. C. Cox and W. Munk, *Slopes of the Sea Surface Deduced from Photographs of Sun Glitter* (Scripps Institution of Oceanography, 1956).
31. P. W. Zhai, Y. Hu, J. Chowdhary, C. R. Trepte, P. L. Luckner, and D. B. Josset, "A vector radiative transfer model for coupled atmosphere and ocean systems with a rough interface," *J. Quant. Spectrosc. Radiat. Transfer* **111**, 1025–1040 (2010).
32. M. Sancer, "Shadow-corrected electromagnetic scattering from a randomly rough surface," *IEEE Trans. Antennas Propag.* **17**, 577–585 (1969).
33. K. J. Voss and N. Souaidia, "POLRADs: polarization radiance distribution measurement system," *Opt. Express* **18**, 19672–19680 (2010).
34. J. Chowdhary, B. Cairns, and L. D. Travis, "Contribution of water-leaving radiances to multiangle, multispectral polarimetric observations over the open ocean: bio-optical model results for case 1 waters," *Appl. Opt.* **45**, 5542–5567 (2006).
35. M. Chami, R. Santer, and E. Dilligeard, "Radiative transfer model for the computation of radiance and polarization in an ocean-atmosphere system: polarization properties of suspended matter for remote sensing," *Appl. Opt.* **40**, 2398–2416 (2001).
36. E. P. Zege and L. I. Chaikovskaya, "New approach to the polarized radiative transfer problem," *J. Quant. Spectrosc. Radiat. Transfer* **55**, 19–31 (1996).
37. G. W. Kattawar and C. N. Adams, "Stokes vector calculations of the submarine light field in an atmosphere-ocean with scattering according to a Rayleigh phase matrix: effect of interface refractive index on radiance and polarization," *Limnol. Oceanogr.* **34**, 1453–1472 (1989).
38. G. Zibordi, S. B. Hooker, J. F. Berthon, and D. D'Alimonte, "Autonomous above-water radiance measurements from an offshore platform: a field assessment experiment," *J. Atmos. Ocean. Technol.* **19**, 808–819 (2002).
39. J. T. Adams and D. J. Gray, "Neutral points in an atmosphere-ocean system. 2: downwelling light field," *Appl. Opt.* **50**, 335–346 (2011).
40. C. Emdo, R. Buras, B. Mayer, and M. Blumthaler, "The impact of aerosols on polarized sky radiance: model development, validation, and applications," *Atmos. Chem. Phys.* **10**, 383–396 (2010).
41. A. A. Lacis, J. Chowdhary, M. I. Mishchenko, and B. Cairns, "Modeling errors in diffuse-sky radiation: vector vs. scalar treatment," *Geophys. Res. Lett.* **25**, 135–138 (1998).
42. D. A. Aurin, H. M. Dierssen, M. S. Twardowski, and C. S. Roessler, "Optical complexity in Long Island Sound and implications for coastal ocean color remote sensing," *J. Geophys. Res.* **115**, C07011 (2010).
43. O. Dubovik and M. D. King, "A flexible inversion algorithm for retrieval of aerosol optical properties from sun and sky radiance measurements," *J. Geophys. Res.* **105**, 20673–20696 (2000).
44. N. T. O'Neill, T. F. Eck, A. Smirnov, B. N. Holben, and S. Thulasiraman, "Spectral discrimination of coarse and fine mode optical depth," *J. Geophys. Res.* **108**, 4559 (2003).
45. B. N. Holben, D. Tanré, A. Smirnov, T. F. Eck, I. Slutsker, N. Abuhassan, W. W. Newcomb, J. S. Schafer, B. Chatenet, F. Lavenue, Y. J. Kaufman, J. V. Castle, A. Setzer, B. Markham, D. Clark, R. Frouin, R. Halthore, A. Karneli, N. T. O'Neill, C. Pietras, R. T. Pinker, K. Voss, and G. Zibordi, "An emerging ground-based aerosol climatology: aerosol optical depth from AERONET," *J. Geophys. Res.* **106**, 12067–12097 (2001).
46. K. T. Whitby, "The physical characteristics of sulfur aerosols," *Atmos. Environ.* **12**, 135–159 (1978).
47. C. Junge, "The size distribution and aging of natural aerosols as determined from electrical and optical data on the atmosphere," *J. Meteorol.* **12**, 13–25 (1955).
48. C. E. Junge, *Air Chemistry and Radioactivity* (Academic, 1963).
49. Y. J. Kaufman, A. Smirnov, B. N. Holben, and O. Dubovik, "Baseline maritime aerosol: methodology to derive the optical thickness and scattering properties," *Geophys. Res. Lett.* **28**, 3251–3256 (2001).
50. P. N. Francis, P. Hignett, and J. P. Taylor, "Aircraft observations and modeling of sky radiance distributions from aerosol during TARFOX," *J. Geophys. Res.* **104**, 2309–2319 (1999).
51. O. Dubovik, A. Smirnov, B. N. Holben, M. D. King, Y. J. Kaufman, T. F. Eck, and I. Slutsker, "Accuracy assessments of aerosol optical properties retrieved from Aerosol Robotic Network (AERONET) sun and sky radiance measurements," *J. Geophys. Res.* **105**, 9791–9806 (2000).
52. J. L. Deuze, P. Goloub, M. Herman, A. Marchand, G. Perry, S. Susana, and D. Tanre, "Estimate of the aerosol properties over the ocean with POLDER," *J. Geophys. Res.* **105**, 15329–15346 (2000).
53. I. Veselovskii, A. Kolgotin, V. Griaznov, D. Müller, K. Franke, and D. N. Whiteman, "Inversion of multiwavelength Raman lidar data for retrieval of bimodal aerosol size distribution," *Appl. Opt.* **43**, 1180–1195 (2004).
54. M. Wang and H. R. Gordon, "Radiance reflected from the ocean-atmosphere system: synthesis from individual components of the aerosol size distribution," *Appl. Opt.* **33**, 7088 (1994).
55. M. Herman, J. L. Deuze, A. Marchand, B. Roger, and P. Lallart, "Aerosol remote sensing from POLDER/ADEOS over the ocean: improved retrieval using a nonspherical particle model," *J. Geophys. Res.* **110**, 1–11 (2005).
56. R. C. Levy, L. A. Remer, D. Tanré, S. Mattoo, and Y. J. Kaufman, "Algorithm for Remote Sensing of Tropospheric Aerosol over Dark Targets from MODIS," Collections 005, and 051: Revision 2 (2009).
57. G. Thuillier, M. Herse, D. Labs, T. Foujols, W. Peetermans, D. Gillotay, P. C. Simon, and H. Mandel, "The solar spectral irradiance from 200 to 2400 nm as measured by the SOLSPEC spectrometer from the ATLAS and EURECA missions," *Solar Phys.* **214**, 1–22 (2003).
58. G. W. Paltridge and C. M. R. Platt, *Radiative Processes in Meteorology and Climatology* (Elsevier, 1976).
59. H. R. Gordon and D. K. Clark, "Clear water radiances for atmospheric correction of coastal zone color scanner imagery," *Appl. Opt.* **20**, 4175–4180 (1981).
60. D. Tanre, M. Herman, P. Y. Deschamps, and A. Deleffe, "Atmospheric modeling for space measurements of ground reflectances, including bidirectional properties," *Appl. Opt.* **18**, 3587–3594 (1979).
61. Y. You, D. Stramski, M. Darecki, and G. W. Kattawar, "Modeling of wave-induced irradiance fluctuations at near-surface depths in the ocean: a comparison with measurements," *Appl. Opt.* **49**, 1041–1053 (2010).
62. Y. You, G. W. Kattawar, K. J. Voss, P. Bhandari, J. Wei, M. Lewis, C. J. Zappa, and H. Schultz, "Polarized light field under dynamic ocean surfaces: numerical modeling compared with measurements," *J. Geophys. Res.* **116**, C00H05 (2011).
63. M. Ottaviani, R. Spurr, K. Stamnes, W. Li, W. Su, and W. Wiscombe, "Improving the description of sunglint for accurate prediction of remotely sensed radiances," *J. Quant. Spectrosc. Radiat. Transfer* **109**, 2364–2375 (2008).
64. S. Kay, J. Hedley, S. Lavender, and A. Nimmo-Smith, "Light transfer at the ocean surface modeled using high resolution sea surface realizations," *Opt. Express* **19**, 6493–6504 (2011).
65. S. Kay, J. D. Hedley, and S. Lavender, "Sun glint correction of high and low spatial resolution images of aquatic scenes: a review of methods for visible and near-infrared wavelengths," *Remote Sensing* **1**, 697–730 (2009).

REPORT DOCUMENTATION PAGE				Form Approved OMB No. 0704-0188	
<p>The public reporting burden for this collection of information is estimated to average 1 hour per response, including the time for reviewing instructions, searching existing data sources, gathering and maintaining the data needed, and completing and reviewing the collection of information. Send comments regarding this burden estimate or any other aspect of this collection of information, including suggestions for reducing the burden, to the Department of Defense, Executive Service and Communications Directorate (0704-0188). Respondents should be aware that notwithstanding any other provision of law, no person shall be subject to any penalty for failing to comply with a collection of information if it does not display a currently valid OMB control number.</p> <p>PLEASE DO NOT RETURN YOUR FORM TO THE ABOVE ORGANIZATION.</p>					
1. REPORT DATE (DD-MM-YYYY) 12-26-2012		2. REPORT TYPE Journal Article		3. DATES COVERED (From - To)	
4. TITLE AND SUBTITLE Polarization Impacts on the Water-leaving Radiance Retrieval from Above-water Radiometric Measurements				5a. CONTRACT NUMBER	
				5b. GRANT NUMBER	
				5c. PROGRAM ELEMENT NUMBER 0602435N	
6. AUTHOR(S) Tristan Harmel, Alexander Gilerson, Alberto Tonizzo, Jacek Chowdhary, Alan Weidemann, Robert Amone and Sam Ahmed				5d. PROJECT NUMBER	
				5e. TASK NUMBER	
				5f. WORK UNIT NUMBER 73-6289-02-5	
7. PERFORMING ORGANIZATION NAME(S) AND ADDRESS(ES) Naval Research Laboratory Oceanography Division Stennis Space Center, MS 39529-5004				8. PERFORMING ORGANIZATION REPORT NUMBER NRL/JA/7323-12-1456	
9. SPONSORING/MONITORING AGENCY NAME(S) AND ADDRESS(ES) Office of Naval Research One Liberty Center 875 North Randolph Street, Suite 1425 Arlington, VA 22203-1995				10. SPONSOR/MONITOR'S ACRONYM(S) ONR	
				11. SPONSOR/MONITOR'S REPORT NUMBER(S)	
12. DISTRIBUTION/AVAILABILITY STATEMENT Approved for public release, distribution is unlimited.					
13. SUPPLEMENTARY NOTES					
14. ABSTRACT <p>Above-water measurements of water-leaving radiance are widely used for water-quality monitoring and ocean-color satellite data validation. Reflected skylight in above-water radiometry needs to be accurately estimated prior to derivation of water-leaving radiance. Up-to-date methods to estimate reflection of diffuse skylight on rough sea surfaces are based on radiative transfer simulations and sky radiance measurements. But these methods neglect the polarization state of the incident skylight, which is generally highly polarized. In this paper, the effects of polarization on the sea surface reflectance and the subsequent water-leaving radiance estimation are investigated. We show that knowledge of the polarization field of the diffuse skylight significantly improves above-water radiometry estimates. In particular in the blue part of the spectrum where the reflected skylight is dominant. A newly developed algorithm based on radiative transfer simulations including polarization is described. Its application to the standard Aerosol Robotic Network-Ocean Color and hyperspectral radiometric measurements of the 1.5-year dataset acquired at the Long Island Sound site demonstrates the noticeable importance of considering polarization for water-leaving radiance estimation. In particular it is shown, based on time series of collocated data acquired in coastal waters, that the azimuth range of measurements leading to good-quality data is significantly increased, and that these estimates are improved by more than 12% at 413 nm.</p>					
15. SUBJECT TERMS water-leaving radiance, sea surface reflection, hyperspectral, polarization					
16. SECURITY CLASSIFICATION OF:			17. LIMITATION OF ABSTRACT UU	18. NUMBER OF PAGES 17	19a. NAME OF RESPONSIBLE PERSON Alan Weidemann
a. REPORT Unclassified	b. ABSTRACT Unclassified	c. THIS PAGE Unclassified			19b. TELEPHONE NUMBER (include area code) 228-688-6232